Check for updates

small methods
www.small-methods.com

Low-Impedance Hybrid Carbon Structures on SiO_X: A Sequential Gas-Phase Coating Approach

Xiaoguang Zhang, Mingcai Zhao, Carlos M. Costa, Juan Zhang, Frieder Scheiba, Senentxu Lanceros-Méndez, Wei Wang, and Qi Zhang*

Carbon coating on SiO_X surface is crucial for enhancing initial Coulombic efficiency (ICE) and cycling performance in batteries, while also buffering volume expansion. Despite its market prevalence, the effects of the carbon layer's quality and structure on the electrochemical properties of SiO_X remain underexplored. This study compares carbon layers produced via gas-phase and solid-phase coating methods, introducing an innovative technique that sequentially uses two gases to develop a low-impedance hybrid carbon structure. In this approach, C_3H_8 is first deposited to create a short-range, vertically ordered carbon architecture, followed by C_2H_2 to establish a long-range, layered structure, effectively filling the gaps. This results in a dense hybrid carbon layer characterized by minimal defects, high crystallinity, and excellent electronic conductivity. The dominant vertical configuration enhances Li-ion migration. The $SiO@C_3H_8@C_2H_2$ prepared through this method yields a specific surface area of 1.14 $m^2\ g^{-1}$ and a high reversible capacity of 1574.9 mAh g^{-1}, alongside an ICE of 83.7%. It showcases remarkable cycling stability, retaining 86.6% capacity after 1000 cycles at room temperature, and performs effectively under varied temperatures and discharging conditions. This low-impedance carbon structure provides a significant reference for other anodes that also require a carbon layer.

1. Introduction

Due to its advantages of high energy density, low self-discharge rate, absence of memory effect, and affordability, lithium-ion batteries (LIBs) have become widely used in electronic products, electric vehicles, and large-scale smart power equipment.[1–3] However, the theoretical capacity of the commercial graphite anodes currently used in LIBs is limited to 372 mAh g^{-1}[4,5] which falls short of meeting the growing demand for higher energy density.[6] Since enhancing the capacity of anode materials is a key strategy to improve the energy density of LIBs, silicon monoxide (SiO_X, $0<x<2$) has emerged as one of the most promising anode materials, attracting significant attention.[7,8] Typically produced through the high-temperature treatment of a silica/silicon mixture, followed by gasification, cooling, and deposition, SiO_X materials exhibit stable cycling performance, a high theoretical specific capacity of ≈2400 mAh g^{-1}, and compatibility with existing LIB anode production systems. Consequently, SiO_X is considered a crucial pathway for the commercial development of high-energy-density batteries for both electronic products and electric vehicles.

The cycling stability of SiO_X is enhanced due to its reduced volume expansion during lithiation and delithiation, which is

X. Zhang, W. Wang
College of Mechanical and Electrical Engineering
Nanjing University of Aeronautics and Astronautics
Nanjing 210016, China

M. Zhao, S. Lanceros-Méndez, Q. Zhang
BCMaterials
Basque Centre for Materials
Applications and Nanostructures; UPV/EHU Science Park
Leioa 48940, Spain
E-mail: mingcaizhao@nuaa.edu.cn

C. M. Costa, S. Lanceros-Méndez
Physics Centre of Minho and Porto Universities (CF-UM-UP) and Laboratory of Physics for Materials and Emergent Technologies
LapMET
University of Minho
Braga 4710-057, Portugal

C. M. Costa
Institute of Science and Innovation for Bio-Sustainability (IB-S)
University of Minho
Braga 4710-053, Portugal

J. Zhang
Jiangsu E-ontech company
Nanjing 210016, China

F. Scheiba
Institute for Applied Materials (IAM)
Karlsruhe Institute of Technology (KIT)
Herrmann-von-Helmholtz-Platz 1, 76344 Eggenstein-Leopoldshafen, Germany

S. Lanceros-Méndez, Q. Zhang
IKERBASQUE
Basque Foundation for Science
Plaza Euskadi, 5, Bilbao 48009, Spain

The ORCID identification number(s) for the author(s) of this article can be found under https://doi.org/10.1002/smtd.202401829

DOI: 10.1002/smtd.202401829

 © 2025 Wiley-VCH GmbH

≈200%, compared to about the 300% expansion seen in pure silicon.[9] This reduced volume change is primarily because the silicon grains within SiO_X are only a few nanometers in size, and the lithium oxide and lithium silicate formed during the initial lithiation create a grid-like network that restrains silicon's volume expansion and prevents rupture. The chemical Si—O bonds between silicon nanocrystals and silica matrix contribute to a robust structure, that is resistant to fracturing. Achieving silicon grains of several nanometers, as found in SiO_X is extremely challenging in pure silicon materials. Additionally, pure silicon/carbon composite anodes are typically only physically mixed, without Si—C bonds, leading to lower structural density, reduced mechanical strength, and increasing susceptibility to rupture. SiO_X's dense structure supports long-term cycling stability and high compaction density, allowing for the use of micron-sized particles, which simplifies manufacturing.[10] However, its initial Coulombic efficiency (ICE) is reduced due to difficulties in extracting Li-ions from the formed lithium oxide and lithium silicate. Additional challenges include low electrical conductivity, poor rate performance, interactions with liquid electrolytes, and the impact of volume expansion on the conductive network, which limits its direct use as an anode material.[11,12]

Coating a uniform carbon layer on SiO_X surfaces is an effective method to mitigate the challenges associated with its use. This carbon layer modifies the numerous pores, cracks, and defects on the crushed surfaces of SiO_X particles, reducing the specific surface area (SSA) and surface energy, which lowers particle surface activity. It also accommodates volume expansion during cycling, enhances electrical conductivity, and significantly reduces interfacial impedance.[13,14] Furthermore, the carbon layer prevents direct contact between SiO_X particles and liquid electrolytes, leading to a more stable solid electrolyte interface (SEI) that consumes less electrolyte and lithium ions.[15] These advancements contribute to improved electrochemical performance, particularly in terms of ICE and long-term cycling stability.

The quality of the carbon layer is greatly influenced by the choice of carbon source and coating method. There are two primary coating techniques: solid-phase and gas-phase. In the solid-phase method, SiO_X particles are mixed with a powdered carbon source and carbonized at high temperatures. In contrast, the gas-phase method deposits carbon onto the SiO_X surface by decomposing a gaseous carbon source at elevated temperatures. Each method offers distinct advantages, playing a crucial role in enhancing the performance of carbon coatings.

This study investigates the influence of carbon layer structure on the performance of SiO_X materials, addressing a gap in the literature where few studies have thoroughly explored this relationship. Both solid-phase and gas-phase coating methods were employed, using coal tar pitch powder for solid-phase coating, and C_3H_8 and C_2H_2 as gaseous carbon sources. The research compares the effects of sequential versus single-gas deposition. Characterization techniques, such as SEM, TEM, XPS, and CS analysis were used to examine the physical properties of the carbon layers. The electrochemical performance of the coated SiO_X was evaluated using coin half-cells, with long-term cycling tests conducted in commercial cylindrical batteries, pairing SiO_x anodes with NCM523 ($LiNi_{0.5}Co_{0.2}Mn_{0.3}O_2$) cathodes.

2. Experimental Section

2.1. Materials Preparation

In this study, a gas-phase coating method, dynamic Chemical Vapor Deposition (CVD) (**Figure 1a**),[16] is used to deposit a carbon layer on the surface of SiO_X micron particles (E-ontech, China). The quality of carbon layers was evaluated using different gaseous carbon sources—C_2H_2, C_3H_8, and their combinations. For comparison, a solid-phase coating method, dynamic stirring (Figure 1b), was also used to apply carbon layers to the SiO_X particles, with coal tar pitch powders (Wuhai New Energy Materials Co., Ltd, China) as the carbon source.

The specific process of the dynamic CVD method is as follows: First, 200 g of SiO_X material was placed in a tube furnace, and the temperature was increased at a rate of 10 °C min^{-1} under a high-purity nitrogen (99.999%) atmosphere. Once the temperature reached 800 °C, a gaseous carbon source was introduced at a flow rate of 40 mL min^{-1} for 30 min. The samples prepared with a single carbon source, C_2H_2 or C_3H_8, were designated as $SiO@C_2H_2$ and $SiO@C_3H_8$, respectively. For a combined process, where C_2H_2 was passed for the first 15 min followed by C_3H_8 for the next 15 min, the resulting sample was denoted as $SiO@C_2H_2@C_3H_8$. In the reverse sequence, it was labeled $SiO@C_3H_8@C_2H_2$.During the gas cracking process, the furnace tube rotated at a speed of 50 r min^{-1}, causing the SiO_X particles to move up and down, ensuring a more uniform carbon layer formation compared to the traditional static method.

The dynamic solid-coating process was carried out as follows: 200 g of SiO_X material and 40 g of pitch powder were thoroughly mixed and placed into a heating-stirring apparatus. The temperature was then increased at a rate of 10 °C min^{-1} under a high-purity nitrogen (99.999%) atmosphere, with the mixing shaft rotating at 120 r min^{-1}. Once the temperature reached 300 °C, it was maintained for 1 h, as this is the softening point of the pitch, indicated by the thermogravimetric curve in Figure 1c. At this stage, the pitch exhibits sufficient fluidity, allowing a uniform carbon layer to form on the SiO_X particle surfaces. Subsequently, the temperature was raised to 800 °C and held for 30 min, allowing the pitch to fully carbonize as shown in Figure 1c. The resulting sample was labeled SiO@Pitch.

The choice of 800 °C for both processes was based on several reasons: First, above 800 °C, two gas-phase carbon sources and the pitch powder were able to carbonize well. However the higher the temperature, the more complete the charring would be. However, SiO_X underwent disproportionation reactions at high temperatures, and the higher the temperature and the longer the duration, the larger the grain size would grow. Figure S1a,b (Supporting Information) shows the XRD curves and corresponding average silicon grain sizes of SiO_X from 800 to 950 °C, respectively. From the figure, it could be seen that the average grain size is the smallest at 800 °C for a short time, at ≈3.6 nm. Importantly, the small grain size could reduce volume changes during charge and discharge cycles.[17]

2.2. Physical and Chemical Characterizations

The particle size distribution of the micron-scale materials was measured using a Laser Particle Size Analyzer (LPSA) (Omec

© 2025 Wiley-VCH GmbH

23669608, 2025, 7, Downloaded from https://onlinelibrary.wiley.com/doi/10.1002/smtd.202401829 by Universidade Do Minho, Wiley Online Library on [27/04/2026]. See the Terms and Conditions (https://onlinelibrary.wiley.com/terms-and-conditions) on Wiley Online Library for rules of use; OA articles are governed by the applicable Creative Commons License

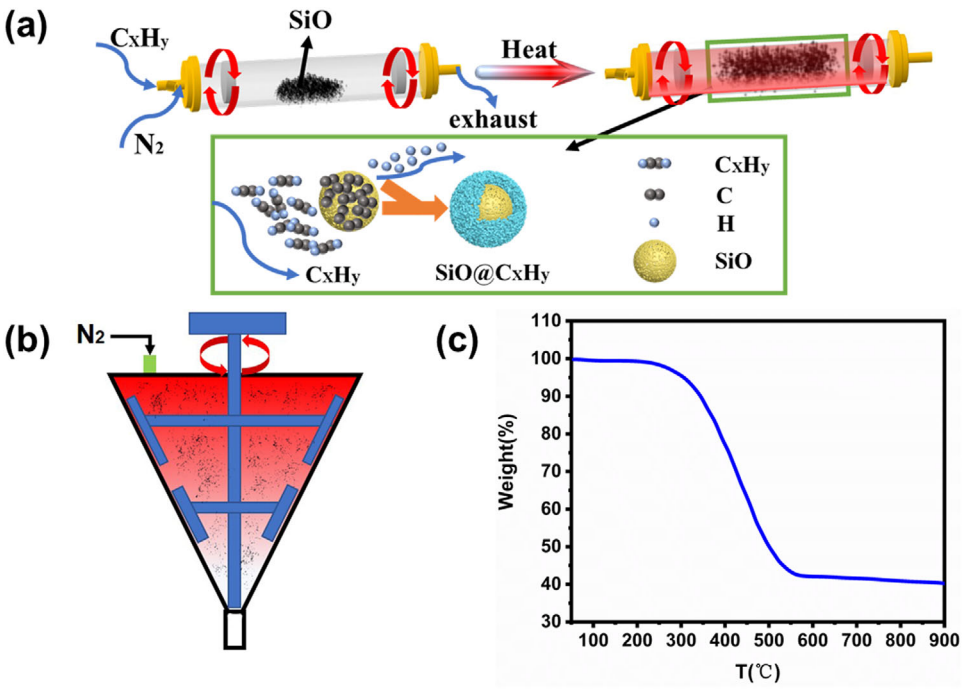


Figure 1. Schematic diagram of a) dynamic gas-phase coating (chemical vapor deposition) method and b) dynamic solid-phase coating method. c) The thermogravimetric curve of coal tar pitch powders.

LS-609), providing data such as D_{10}, D_{50}, and D_{90}. The external morphology and internal structure of the samples were examined using scanning electron microscopy (SEM) (Hitachi S-4800), X-ray diffraction (XRD) (D/max2500 PC), and Raman spectroscopy (Thermo Fisher DXRxi). X-ray photoelectron spectroscopy (XPS) (AXIS Supra) was employed to analyze the elemental composition and chemical states of the surface elements. The carbon content of the samples was determined using a high-frequency infrared carbon-sulfur (C-S) analyzer (N-HW2000A). The specific surface area (SSA) of the samples was measured by a multipoint BET nitrogen adsorption – static capacity method (JWGB BK112). Electrical conductivity was tested using a polarizer resistance tester (BER1300), and interface impedance was measured using an electrochemical workstation (CHI660E). The electrochemical performance of the CR2032-type coin half cells and 18650-type cylindrical full cells was evaluated using the Land Battery Test System (CT2001A).

2.3. Electrochemical Characterizations

CR2032-type coin cells were used for half-cell testing, with the following production process: Active materials (samples), carbon black conductive agent (SP), sodium carboxymethyl cellulose (CMC), and polymerized styrene-butadiene rubber (SBR) were mixed in a mass ratio of 95.8:1:1.4:5.6. The resulting slurry was evenly coated onto a 15 µm thick copper foil. After natural drying, the coated copper foil was placed in a vacuum oven at 80 °C for 10 h. The foil was then compacted to 75% of its original thickness using a roller press, punched, and cut into 13 mm diameter disks. The half-cells were assembled in a high-purity argon glove box, using lithium metal foils as the counter electrode and polypropylene macroporous films (Celgard 2400) as the separator. The electrolyte was a 1 M $LiPF_6$ solution in a mixture of ethylene carbonate (EC), dimethyl carbonate (DMC), and ethyl methyl carbonate (EMC) (1:1:1 by volume) with 5 wt.% fluorinated ethylene carbonate (FEC).

For the 18650-type cylindrical batteries used in full-cell testing, the production process was as follows: Active materials (samples), SP, CMC, SBR, and deionized water were mixed in a mass ratio of 100:1:1.4:1.4:100 to form the anode slurry. The cathode active material used was $LiNi_{0.5}Co_{0.2}Mn_{0.3}O_2$ (NCM523), with the specific formulation being SP: polyvinylidene fluoride (PVDF): NMP: NCM523 = 1.5:1.5:37:100. The cathode slurry was uniformly coated on both sides of a 15 µm thick aluminum foil, while the anode slurry was coated on an 8 µm thick copper foil. The areal densities of the cathode and anode electrodes were 400 and 200 g m^{-2}, respectively, with compaction densities of 2.87 and 1.65 g cm^{-3}. After slitting, welding lugs, coiling, shelling, welding, rolling grooves, and drying (at 80 °C under vacuum for 12 h), the batteries were filled with electrolyte and underwent further assembly processes to complete the final cylindrical batteries.

3. Result and Discussion

3.1. Morphological Analysis

Figure 2a–f present the surface morphology of SiO_X particles before coating and after coating with different schemes, respectively. Given that SiO_X micron-sized particles are obtained through mechanical crushing, it is evident that the surface exhibits certain defects, such as holes, steps, and particles of a

© 2025 Wiley-VCH GmbH

23669608, 2025, 7, Downloaded from https://onlinelibrary.wiley.com/doi/10.1002/smtd.202401829 by Universidade Do Minho, Wiley Online Library on [27/04/2026]. See the Terms and Conditions (https://onlinelibrary.wiley.com/terms-and-conditions) on Wiley Online Library for rules of use; OA articles are governed by the applicable Creative Commons License

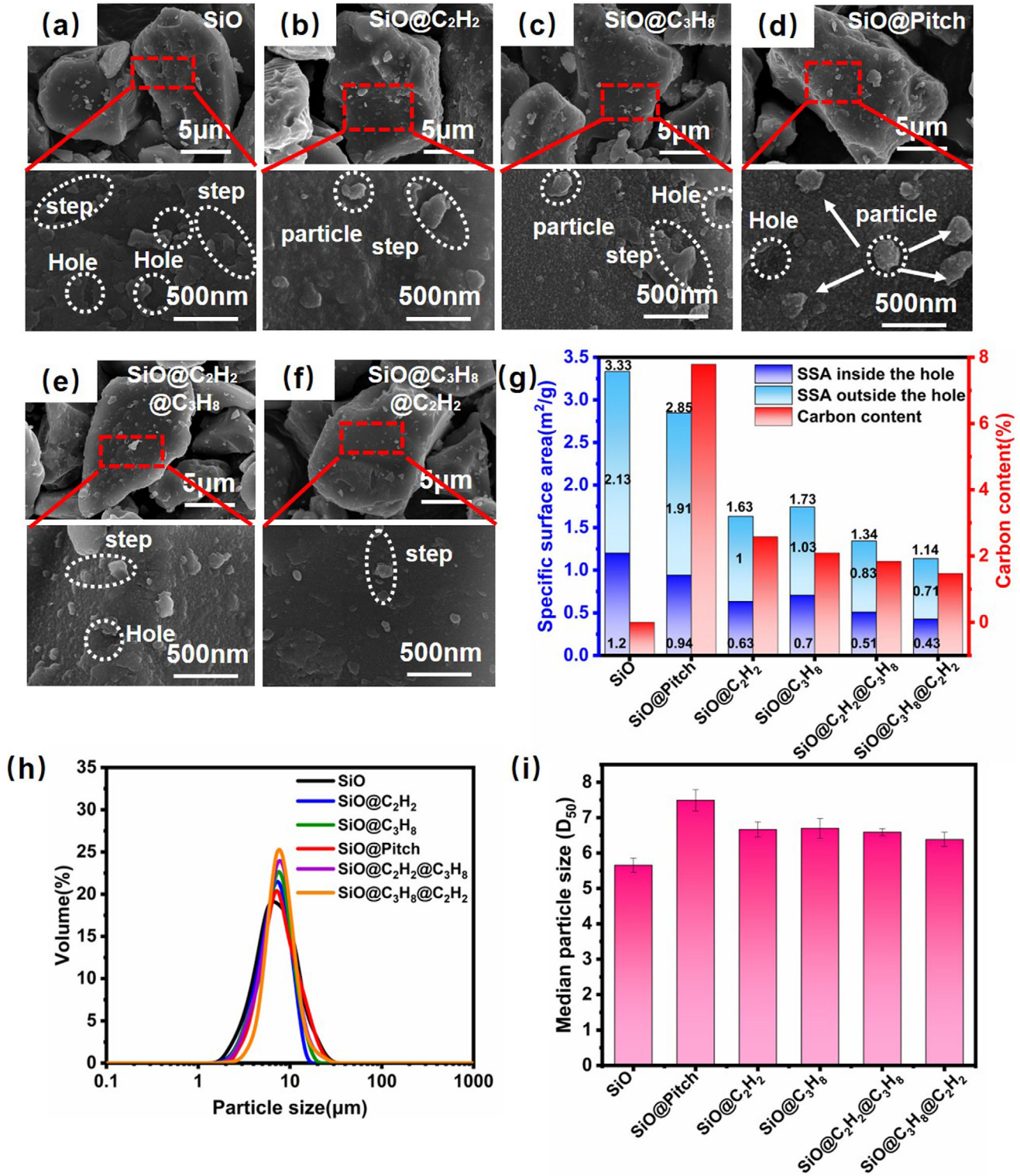


Figure 2. SEM surface morphology of a) SiO_X, b) $SiO@C_2H_2$, c) $SiO@C_3H_8$, d) SiO@pitch, e) $SiO@C_2H_2@C_3H_8$ and f) $SiO@C_3H_8@C_2H_2$ at different magnifications. g) SSA (left vertical axis) and carbon content (right vertical axis) curves, h) Particle size distribution curves, i) Median particle size (D_{50}) of the 6 samples.

© 2025 Wiley-VCH GmbH

23669608, 2025, 7, Downloaded from https://onlinelibrary.wiley.com/doi/10.1002/smtd.202401829 by Universidade Do Minho, Wiley Online Library on [27/04/2026]. See the Terms and Conditions (https://onlinelibrary.wiley.com/terms-and-conditions) on Wiley Online Library for rules of use; OA articles are governed by the applicable Creative Commons License

smaller size. Conversely, since the SiO_X material is a dense substance, the surface remains relatively smooth, with the exception of the aforementioned defects. This can be verified in the test of SSA (Figure 2g), which is relatively low with a SSA of only 3.33 $m^2\ g^{-1}$. After the gas-phase coating process, the surfaces of the samples in Figure 2b,c,e,f retained numerous smaller particles and step-type defects, indicating that the deposited carbon layers were relatively thin and inadequate to cover defects greater than 100 nm. However, it is important to note that the edges of these defects became smoother, resulting in a significant reduction of the SSA of the samples, which decreased to approximately half of its original value (1.63 $m^2\ g^{-1}$ for $SiO@C_2H_2$) or even a third (1.14 $m^2\ g^{-1}$ for $SiO@C_3H_8@C_2H_2$). For comparison, after the solid-phase coating process, the sample in Figure 2d retains a considerable number of smaller particles on its surface and its SSA is still 2.85 $m^2\ g^{-1}$, representing only a 14.4% reduction. This indicates that the gas-phase method, despite exhibiting a lower carbon increase than the solid-phase method, demonstrates superior efficacy in reducing the SSA and is more conducive to the formation of a uniform carbon layer.

Concurrently, the carbon coating has the capacity to adhere hundreds of nanometer-sized SiOx particles to the surface of micron-sized particles, thereby reducing the SSA, narrowing the particle distribution, and increasing the median particle size (D_{50}) of the samples, as illustrated in Figure 2h,i. The observed increase in D_{50} of ≈1 µm for the gas-phase-coated samples and 2 µm for the solid-phase-coated one, which is associated with the larger asphalt particles, which are capable of bonding with larger particles, and even agglomerations. This suggests that the carbon layer formed from pitch is of the lowest quality, with numerous uncovered pores and a discontinuous carbon layer.

SiO_X materials require a uniform carbon layer with low SSA and minimal carbon content, as excessive carbon diminishes the material's specific capacity. Figure 2g indicates that increasing carbon does not necessarily decrease SSA; however, using two gases for sequential coating effectively reduces SSA more than a single gas, even with a lower carbon increment. The $SiO@C_3H_8@C_2H_2$ demonstrates the lowest SSA and carbon content, suggesting this method is optimal for SSA reduction. This more efficient approach allows for reduced C_2H_2 usage, thereby enhancing productivity.

The SSA is categorized into internal and external components (Figure 2g), reflecting pore defects and surface roughness, respectively. Gas diffusion allows penetration into materials, depositing carbon along defects, thus reducing internal SSA. A lower internal SSA minimizes electrolyte intrusion, which in turn reduces the formation of SEI films.[18] It is noted that C_2H_2 is more effective than C_3H_8 in lowering internal SSA, with measurements indicating $SiO@C_2H_2$ achieves 0.63 $m^2\ g^{-1}$ compared to 0.70 $m^2\ g^{-1}$ for $SiO@C_3H_8$. When C_2H_2 is the last gas passed in $SiO@C_3H_8@C_2H_2$, the internal SSA is reduced to 0.43 $m^2\ g^{-1}$, which is lower than the 0.51 $m^2\ g^{-1}$ of $SiO@C_2H_2@C_3H_8$, where C_3H_8 is the last gas. The gases produce different cracking polycyclic aromatic hydrocarbons (PAHs) as by-products, with C_2H_2 yielding smaller, more penetrative molecules PAHs ($C_{13}H_{12}$) that facilitate deeper pore filling, whereas C_3H_8 generates larger, more aggregative molecules PAHs ($(C_6H_5)_3CH$) that predominantly cover surface defects.[19–21] This differential influence underscores the importance of gas selection and sequence in effectively minimizing internal SSA.

3.2. Structural Analysis

Figure 3a,b present a comparison of the internal structures of carbon layers deposited on SiO_X surfaces using C_2H_2 and C_3H_8. The carbon layer from C_2H_2, depicted in Figure 3a, shows elongated lattice stripes parallel to the SiO_X surface, forming a graphite-like structure with high crystallinity. In contrast, the layer obtained from C_3H_8, illustrated in Figure 3b, reveals shorter, perpendicular lattice stripes that are characterized by small grains within an amorphous matrix and lower crystallinity. These structural differences arise from the distinct carbon atom arrangements during the gas cracking process; Acetylene (C_2H_2), with its high-energy and not easily breakable C≡C bonds, facilitates a layered structure, while the lower-energy and easily breakable C—C bonds in propane (C_3H_8) result in a less ordered, vertical chain formation.[22,23] Furthermore, Figure 3c depicts a carbon layer produced from pitch, which is thicker and predominantly amorphous, with minimal crystalline structure noticeable.

The TEM images in Figure 3d,e demonstrate the structural differences in carbon layers formed by sequential deposition of C_2H_2 and C_3H_8. Figure 3d depicts a graphite-like layered structure resulting from initial C_2H_2 deposition, subsequently overlaid by C_3H_8, which forms a vertical structure. Conversely, Figure 3e reveals that the initial deposition of C_3H_8 creates vertical grains, while the addition of C_2H_2 yields a layered structure between and on the surface of these vertical grains. The resulting carbon layers from the gas method exhibit a bilayer-like structure, where the carbon from C_2H_2 shows long-range order and layering, and that from C_3H_8 displays vertical alignment and short-range order. Notably, the configuration where C_2H_2 is deposited first creates a distinct bilayer structure with horizontal lattices below and vertical lattices above, whereas the reverse order results in a more intricate double-layered structure due to the interference of C_3H_8's discontinuous vertical lattices. The crystalline carbons present a layer spacing between 0.3371 and 0.3378 nm, corresponding to the C (002) diffraction peak.[24] These crystalline structures enhance electronic conductivity and reduce the impedance of SiO_X. Additionally, the crystallinity, orientation of the carbon nanocrystals, and layer spacing significantly impact the Li-ion migration rate.[25,26]

Based on the characteristics of the carbon layers formed from the gases C_2H_2 and C_3H_8, Figure 3f illustrates a schematic diagram of how the carbon layer forms with different orders of their deposition. Introducing C_2H_2 first results in a continuous horizontal layer on the SiO_X surface, while subsequent C_3H_8 deposition creates a discontinuous vertical layer. If C_3H_8 is deposited first, it leads to a discontinuous vertical structure, into which the PAHs and carbon particles from later C_2H_2 deposition fill the gaps, resulting in a denser layer. When Li-ions migrate through these carbon layers to SiO_X, the impediment along the interlayer of the vertical grains is much smaller than across the interlayer of the layered grains. However, a vertically structured carbon layer formed solely from C_3H_8 deposition tends to have gaps, exposing more SiO_X directly to the liquid electrolyte and potentially

© 2025 Wiley-VCH GmbH

23669608, 2025, 7, Downloaded from https://onlinelibrary.wiley.com/doi/10.1002/smtd.202401829 by Universidade Do Minho, Wiley Online Library on [27/04/2026]. See the Terms and Conditions (https://onlinelibrary.wiley.com/terms-and-conditions) on Wiley Online Library for rules of use; OA articles are governed by the applicable Creative Commons License

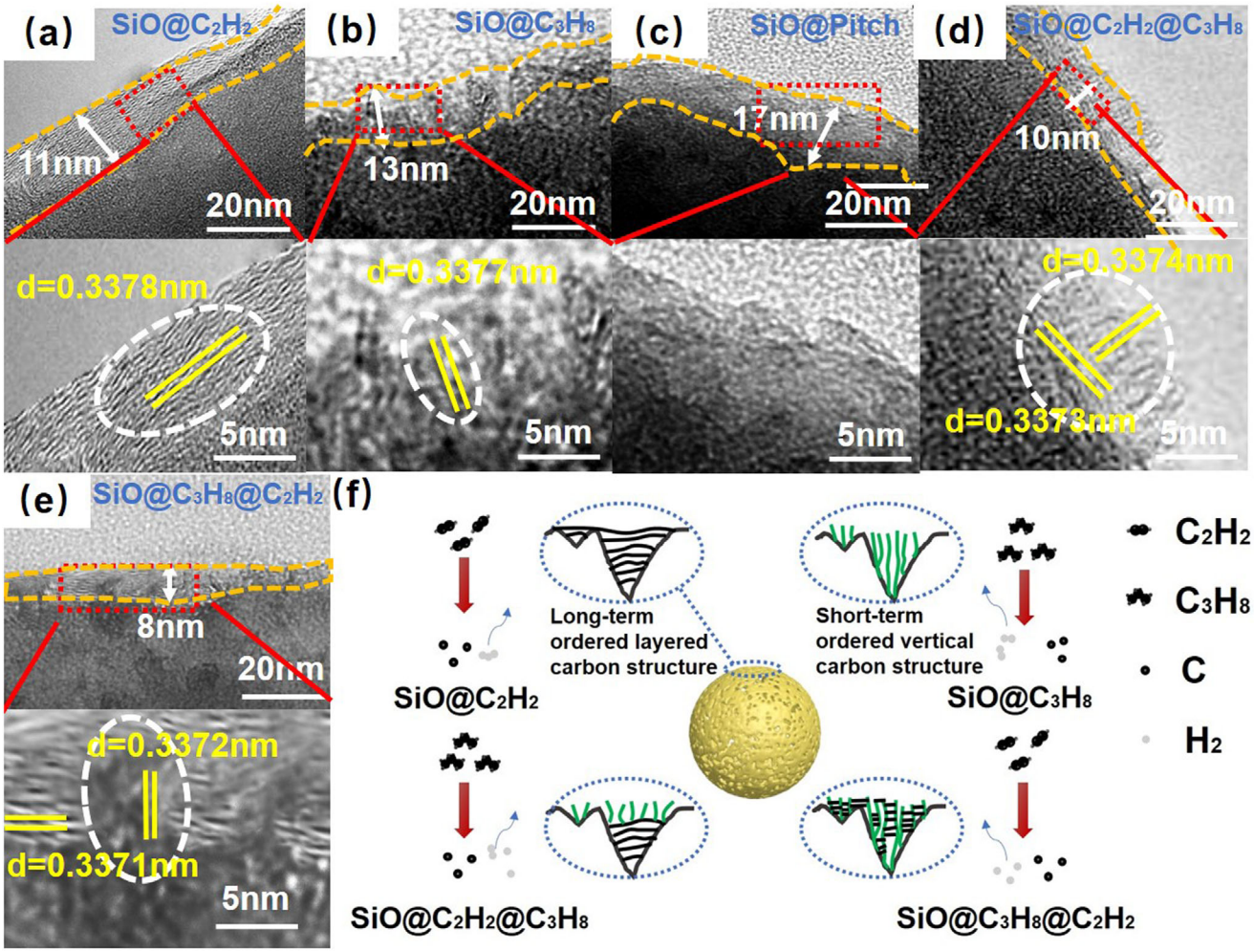


Figure 3. TEM images of a) $SiO@C_2H_2$, b) $SiO@C_3H_8$, c) SiO@pitch, d) $SiO@C_2H_2@C_3H_8$, and e) $SiO@C_3H_8@C_2H_2$ at different magnifications. f) Schematic diagram of carbon layers formed by the successive deposition of C_2H_2 and C_3H_8 in different sequences.

compromising overall performance. Thus, the strategic sequencing of C_2H_2 after C_3H_8 optimizes carbon layer integrity and functionality.

Figure 4a presents the X-ray diffraction (XRD) patterns for various samples. The raw SiO_X material shows a broad peak indicative of its structure. After high-temperature coating, distinct Si peaks appear at 2Theta values of 28.44° (111), 47.31° (220), and 56.12° (311), resulting from the structural instability of SiO_X, which undergoes a disproportionation reaction to form Si and silica nanoparticles.[27,28] Notably, no silicon carbide (SiC) peaks are observed, suggesting that silicon does not react with carbon under these conditions. The average Si grain sizes in SiO_X, $SiO@C_2H_2$, $SiO@C_3H_8$, SiO@Pitch, $SiO@C_2H_2@C_3H_8$, and $SiO@C_3H_8@C_2H_2$, calculated using the Scherrer formula, are 2.3, 5.1, 4.8, 5.5, 4.7, and 4.5 nm for the respective samples, indicating that silicon grain size generally increases post-disproportionation during high-temperature treatment. The consistent duration of treatment across all carbon-coated processes results in minimal variation in grain sizes of $\approx 5 \pm 0.5$ nm, which minimizes variations due to different properties of the SiO_X materials.

Figure 4b presents the Raman spectra for various samples, highlighting the characteristic peaks at 517 cm^{-1} for crystalline Si (c-Si) and at 1350 cm^{-1} (D band) and 1580 cm^{-1} (G band) for carbon materials. The D band correlates with lattice defects linked to sp^3 hybridized carbon, while the G band reflects in-plane stretching of sp^2 hybridized carbon. The intensity ratio of these bands denoted as I_D/I_G, serves as an indicator of defect levels within the carbon structure, with higher ratios signifying more defects.[29] The SiO@Pitch sample displays the highest I_D/I_G ratio of 1.23, indicating significant defects in the carbon layer formed from pitch. Conversely, samples treated with gaseous carbon sources reported lower I_D/I_G ratios, suggesting improved quality and fewer defects. Among these, the sequential gas treatment of $SiO@C_3H_8@C_2H_2$ yielded the lowest ratio of 0.88, indicating superior crystallinity and reduced defects, thereby suggesting enhanced conductivity.[30,31] This observation is further supported by TEM analysis in Figure 3f, which demonstrates a more ordered and defect-free carbon layer resulting from the sequential use of C_3H_8 followed by C_2H_2.

The quality of a carbon layer can be evaluated by its elemental composition, with a more uniform layer indicating fewer defects

© 2025 Wiley-VCH GmbH

23669608, 2025, 7, Downloaded from https://onlinelibrary.wiley.com/doi/10.1002/smtd.202401829 by Universidade Do Minho, Wiley Online Library on [27/04/2026]. See the Terms and Conditions (https://onlinelibrary.wiley.com/terms-and-conditions) on Wiley Online Library for rules of use; OA articles are governed by the applicable Creative Commons License

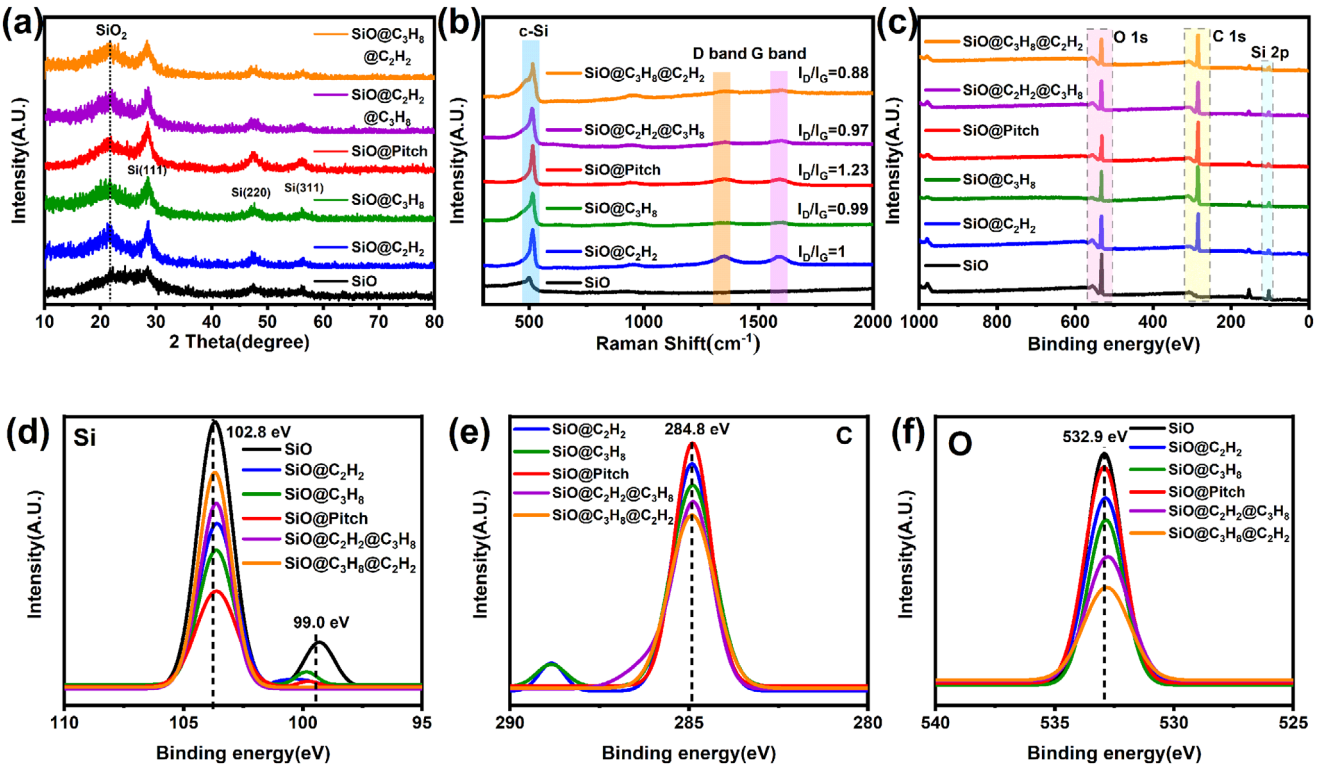


Figure 4. a) XRD spectrum b) Raman spectrum c) XPS spectrum d) Si 2p absorption peak e) C 1s absorption peak f) O 1s absorption peak of all samples.

and reduced exposure to other elements. X-ray Photoelectron Spectroscopy (XPS) is effective for analyzing surface elemental distribution, revealing insights within a few nanometers of the surface. The primary elemental constituents identified include silicon (Si), carbon (C), and oxygen (O), with distinct XPS peaks in Figure 4d–f. In Figure 4d, the peak ≈99.1 eV corresponds to the Si 2p absorption peak of elemental silicon, while the peak at ≈102.8 eV represents silicon oxide. Both peaks decrease in intensity after carbon coating, with the gas-phase method showing lower intensities than the solid-phase method. These reductions are attributed to the more uniform carbon encapsulation provided by the gas-phase method compared to the solid-phase method, although the intensity of the C 1s peak of the solid-phase method is highest in Figure 4e.

The electrochemical performance of SiO_X anode materials is significantly influenced by their oxygen content. The higher oxygen content can reduce the proportion of electrochemically active lithium storage phases (such as $Li_{13}Si_4$), increase the number of irreversible phases like Li_2O and Li_4SiO_4, and decrease the initial Coulombic efficiency. As shown in Figure 4f, there is a significant decrease in the O 1s peak intensity for all carbon-coated samples compared to the raw SiO_X material, and the smaller the SSA, the lower the O 1s peak intensity, indicating that the higher the quality of the carbon layer, the more effective it is in reducing exposure of oxygen. Meanwhile, the higher ratio of the intensity of the singlet Si 2p peak to the silicon oxide in Figure 4d indicates a greater proportion of elemental silicon relative to silicon oxide in the SiO_X after disproportionation.[32,33] This is related to the movement of oxygen atoms toward the SiO_X surface and their reduction by deposited carbon atoms, and a more uniform carbon layer enhances the reduction of oxygen.

3.3. Impedance Analysis

SiO_X materials generally suffer from low electronic and ionic conductivity, which can be effectively improved through carbon coating. Electrochemical impedance spectroscopy (EIS) is obtained by measuring the corresponding current (voltage) response generated through sine wave frequency excitation, which is an important method for studying the electrochemical performance of electrode materials. In this experiment, the frequency range is 0.01 Hz–100 KHz, with an amplitude of 10 mV, a scanning rate of 0.5 mVs^{-1}, and a voltage range of 0–2.0 V. **Figure 5a** displays the electrochemical impedance spectroscopy (EIS) results for all samples in a half-cell configuration, with the equivalent circuit diagram provided in Figure 5b. EIS results indicate that all six samples exhibit semicircles in the mid- and high-frequency regions, alongside diagonal lines in the low-frequency spectrum. The ultra-high frequency range reflects contact impedance (R_c) as Li-ions and electrons move through the electrolyte, porous membrane, and active materials.[34] High-frequency semicircles signify the impedance of the SEI passivation film (R_{SEI}), while the mid-frequency ones indicate charge transfer impedance (R_{ct})[35,36]; the semicircle diameter correlates with charge transfer difficulty, and the larger the diameter, the more difficult the charge transfer is[37] Notably, carbon coating generally reduces this impedance, with gas-phase method outperforming

© 2025 Wiley-VCH GmbH

23669608, 2025, 7, Downloaded from https://onlinelibrary.wiley.com/doi/10.1002/smtd.202401829 by Universidade Do Minho, Wiley Online Library on [27/04/2026]. See the Terms and Conditions (https://onlinelibrary.wiley.com/terms-and-conditions) on Wiley Online Library for rules of use; OA articles are governed by the applicable Creative Commons License

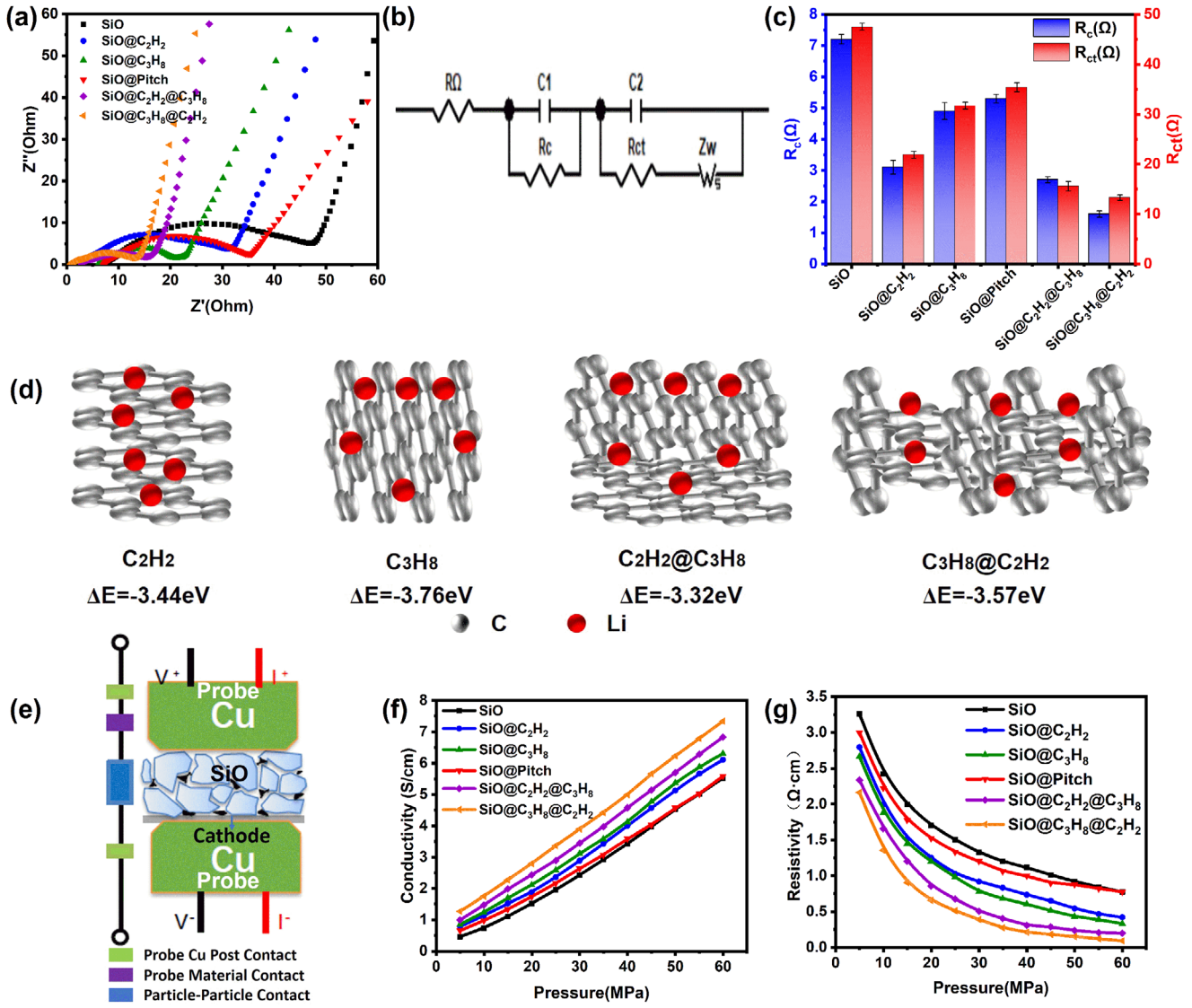


Figure 5. a) Electrochemical impedance spectroscopy b) Equivalent circuit c) Material contact impedance and interface impedance diagram of all samples. d) Schematic diagram of the adsorption model of Li-ions by different carbon layer structures. e) Schematic diagram of resistance tester. f) Polarized conductivity and g) Polar resistivity of the electrode sheet of all samples.

solid-phase methods. Among the samples, those treated with two gases showed lower impedance than a single gas, particularly SiO@C_3H_8@C_2H_2, which exhibited the least impedance values in Figure 5c of 13.3 Ω for R_{ct} and 1.6 Ω for R_c, compared to SiO_X's higher values of 47.5 Ω and 7.2 Ω, respectively.

The diagonal line in the low-frequency region in Figure 5a represents the Warburg impedance (Z_w), which correlates with the diffusion of Li-ions within materials. A steeper slope indicates a lower Z_w, facilitating enhanced Li-ion diffusion.[38] For example, SiO@Pitch exhibits a lower slope compared to SiO_X, likely due to non-uniform pitch powder coating that may have led to partial agglomerates, impeding Li-ion migration.[39] The analysis also shows the slopes of the samples prepared with a single gas do not show significant improvements over SiO_X, while those prepared with two gases exhibit a noticeable increase, suggesting that a bilayer carbon structure reduces the R_{ct} and Z_w effectively. This could be caused by the following reasons. First, the bilayer carbon structure provides a more homogeneous coverage and a more effective reduction of surface SiO_X to Si compared to a single-layer carbon structure. Second, the more uniform carbon layer better buffers the volume change of the SiO_X, maintaining the integrity and stability of the interface with the electrolyte. Finally, different carbon structures or a certain carbon structure is able to optimize the diffusion path of Li-ions, thus reducing the impedance. Lower R_{ct} and Z_w values are advantageous as they reduce kinetic limitations during discharge, leading to a greater depth of lithiation/delithiation in the particles and a decreased concentration gradient of Li-ions between the interior and surface of the particles, ultimately enhancing electrochemical performance.[40] This requires further analysis of the adsorption energy of these carbon layers.

© 2025 Wiley-VCH GmbH

23636608, 2025, 7, Downloaded from https://onlinelibrary.wiley.com/doi/10.1002/smtd.202401829 by Universidade Do Minho, Wiley Online Library on [27/04/2026]. See the Terms and Conditions (https://onlinelibrary.wiley.com/terms-and-conditions) on Wiley Online Library for rules of use; OA articles are governed by the applicable Creative Commons License

The study investigates the adsorption energy of Li-ions on various carbon layer structures using density functional theory (DFT). The adsorption models for Li-ions on various carbon layers are illustrated schematically in Figure 5d, which are based on the carbon layer structures observed in TEM images (Figure 3ab–de), with specific parameters and calculation procedures detailed in the Supplementary Material. The absolute value of the adsorption binding energy (ΔE) reflects the strength of interaction between Li-ions and the carbon layer,[41] and the higher ΔE will enhance the stability of Li-ion storage and minimize self-discharge.[42] However, high binding energy does not necessarily imply high ionic conductivity, as factors such as crystal structure, defect concentration, and ion-channel relationships also play significant roles.[43] Notably, the vertical carbon layer model demonstrates a significantly stronger binding (ΔE of 3.76 eV) than the horizontal model and the hybrid models, suggesting the vertical carbon layer has the best stability with Li-ions. Meanwhile, the impedance of Li-ions migrating along the vertical carbon layer structure is smaller compared to that of Li-ions migrating through the horizontal carbon layer structure. Therefore, all else being equal, the higher the binding energy (ΔE) of the carbon layer, the better its ionic conductivity, given that the carbon layer differs only vertically and horizontally. In the hybrid carbon layer, both structures combine vertical and layered carbon structures, but $SiO@C_3H_8@C_2H_2$ exhibits higher adsorption energy. This is due to the fact that $SiO@C_3H_8@C_2H_2$ is dominated by the first-deposited vertical-structured carbon, which serves as a channel for Li-ion migration, whereas $SiO@C_2H_2C_3H_8$ is dominated by the first-deposited more continuous layered-structured carbon. This finding makes its potential in applications where continuous vertical structures are impractical.

The performance of Li-ion batteries is heavily impacted by resistance, which includes both ionic and electronic components. Electronic resistance of the electrode involves factors such as active material, current collector, and interfacial contact, making it vital to accurately assess these properties to predict the overall resistance of the battery cell.[44] In industry, a controllable voltage probe is employed to measure resistance across the electrode's thickness, with the principle illustrated in Figure 5e. Experimental data in Figure 5f,g indicate that as testing pressure increases, the reduction in pore size within the electrode enhances particle contact, decreasing resistivity and improving conductivity. However, when the pressure exceeds 40 MPa, the resistivity of SiO@Ptich is observed to decline. This decline may be attributed to the low strength and uneven structure of the carbon layer formed by pitch powders, which becomes more susceptible to damage under high pressure. Conversely, gas-phase-coated samples show improved conductivity, with those utilizing two gases yielding superior performance. Notably, $SiO@C_3H_8@C_2H_2$ exhibits the lowest resistivity and highest conductivity, highlighting the efficacy of a hybrid carbon layer structure in mitigating impedance compared to a single-layer approach.

3.4. Half-Cell Performance

Half-cell tests with coin cells are a standard approach for assessing the electrochemical performance of anode and cathode materials, particularly regarding initial Coulombic efficiency (ICE), impedance, and cyclic voltammetric curves (CV). **Figure 6a** shows the first charge and discharge curves and ICE for six samples, with the voltage ranging from 0.01 to 1.5 V and a charge/discharge current density of 0.15 $A{\cdot}g^{-1}$ (0.1C). Figure S2 (Supporting Information) shows the charge curves of all samples. The results indicate that the raw SiO_X material exhibits the highest discharge capacity of 2025.1 mAh g^{-1} but the lowest ICE of only 68.6%. Post-coating with a carbon layer results in slight reductions in discharge capacities, yet significant increases in ICE due to minimized contact between SiO_X and the liquid electrolyte, which conserves Li-ions during SEI formation. Notably, samples utilizing gaseous carbon sources show superior performance compared to those using the solid carbon source, with the best results from dual gas coatings. Specifically, the $SiO@C_3H_8@C_2H_2$ sample achieves the highest ICE of 83.7%, underscoring the advantage of a uniform carbon layer with low SSA in enhancing the capacity and ICE of SiO_X.

Cyclic voltammetry (CV) tests were conducted on samples across a voltage range of 0.01–2.0 V, a scan rate of 0.1 mV s^{-1}, and three scanning cycles. As shown in Figure 6b–g, both raw and coated samples exhibit similar cathodic and anodic peak positions, with arrows indicating the scan direction, representing their lithiation and delithiation processes. Notably, variations in the microstructure of the carbon layer play a crucial role in enhancing Li-ion diffusion kinetics and overall electrochemical performance. During the cathodic scan, a distinct peak at ≈0.01 V indicates the transition from amorphous LixSi ($0 \leq x \leq 3.75$) to crystalline $Li_{15}Si_4$ alloys and the lithiation of carbon materials.[45] In contrast, the anodic scan features a significant peak ≈0.6 V, corresponding to the delithiation of LixSi into amorphous Si.[46,47] The consistency observed between the second and third CV curves demonstrates the cyclability of the samples, with carbon-coated samples showing significant improvements, especially those derived from gaseous carbon sources. And, the two consecutive gases provide better results than a single gas, with $SiO@C_3H_8@C_2H_2$ exhibiting nearly overlapping second and third curves.[48] Cycle performance tests further endorse these findings, showcasing that after 100 cycles, raw SiO_X shows the least effectiveness, whereas carbon-coated samples, particularly $SiO@C_3H_8@C_2H_2$, indicate superior capacity retention and more stable Coulombic efficiency curves (Figure S3, Supporting Information). Although $SiO@C_3H_8@C_2H_2$ demonstrates the best performance in half-cell tests, its true cycling performance should be verified in commercial full-cell applications.

3.5. Full-Cell Performance

Silicon-based batteries exhibit poor cycling performance primarily due to the high consumption of Li-ions and liquid electrolytes. Testing with lithium foil and excess electrolyte can obscure the rapid depletion of Li-ions inherent to those half-cells. In contrast, commercial batteries utilize a standard cathode material and precisely dosed electrolytes, offering a more accurate assessment of active materials' performance. This study investigates the cycling performance of various Si-based materials across different temperatures and discharge multipliers in a commercial 18650-type cylindrical cell. All samples demonstrate specific capacities exceeding 1500 mAh g^{-1}, but their larger volume

© 2025 Wiley-VCH GmbH

23669608, 2025, 7, Downloaded from https://onlinelibrary.wiley.com/doi/10.1002/smtd.202401829 by Universidade Do Minho, Wiley Online Library on [27/04/2026]. See the Terms and Conditions (https://onlinelibrary.wiley.com/terms-and-conditions) on Wiley Online Library for rules of use; OA articles are governed by the applicable Creative Commons License

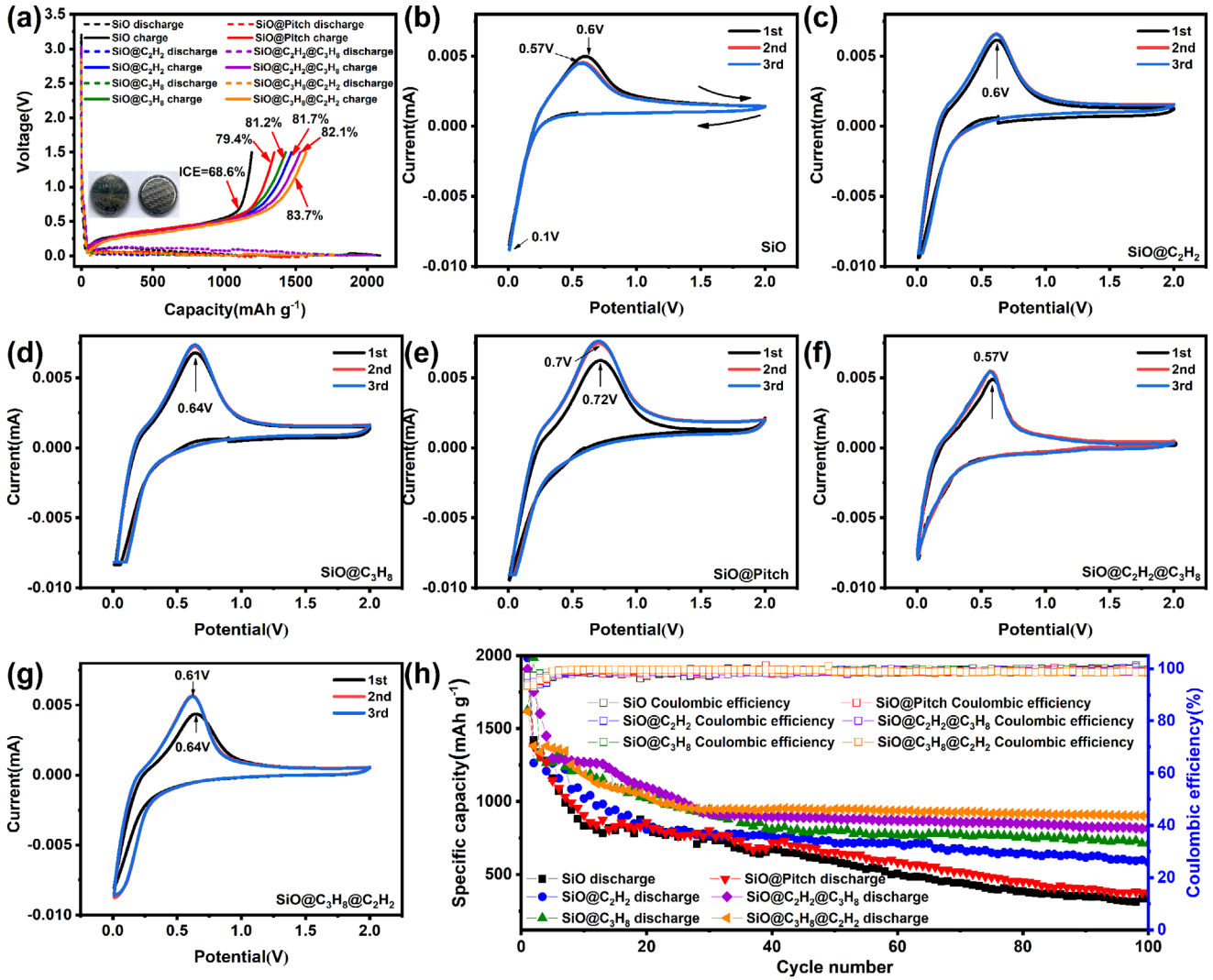


Figure 6. a) Half-cell first charge and discharge curves of all samples. Cyclic voltammetry curve of b) SiO_X, c) $SiO@C_2H_2$, d) $SiO@C_3H_8$, e) SiO@Pitch, f) $SiO@C_2H_2@C_3H_8$, g) $SiO@C_3H_8@C_2H_2$. h) Cycle performance and Coulombic efficiency curves of all samples at room temperature (25 °C).

expansions complicate direct application with current commercial cathodes, which have lower capacities. Consequently, these materials are typically combined with commercial graphite (CG) to achieve a target specific capacity of 420 mAh g^{-1}, the N/P ratio of the full cell is 1.05, with adjusted mixing ratios: SiO_X: CG = 7.7: 92.3, $SiO@C_2H_2$: CG = 5.9: 94.1, $SiO@C_3H_8$: CG = 5.6: 94.4, SiO@Pitch: CG = 6.4: 93.6, $SiO@C_2H_2@C_3H_8$: CG = 5.3: 94.7, and $SiO@C_3H_8@C_2H_2$:CG = 5: 95. The surface density of cathode electrode is 380 g m^{-2} and that of anode electrode is 192.82 g m^{-2}. The first charge and discharge curves and ICE of these mixtures are illustrated in Figure S4 (Supporting Information).

The full-cell tests evaluated batteries within a voltage range of 2.5–4.2 V, employing a charging current density of 0.5C and a discharging current density of 1C. The first charge and discharge curves in **Figure** 7a for all cylindrical battery samples indicate an ICE between 86% and 87%, primarily determined by the lower ICE of the active materials. Since the ICE of the cathode material NCM523 in this experiment falls between 86% and 87% and the ICE of the anode materials (shown in Figure S2, Supporting Information) is above 92%, the ICE of the full battery is close to that of the cathode material. Figure 7b illustrates the discharge performance of the full cells under varying discharge rates, with a charging rate of 0.5C. As the discharge rate increases from 0.5 to 5C, the discharge capacity of the cells decreases. At discharge rates below 3C, the differences in discharge capacity among the samples are minimal, but significant variations emerge at rates above 4C. Gas-coated samples show higher discharge capacities than SiO@Pitch, owing to a more uniform carbon layer, with $SiO@C_3H_8@C_2H_2$ demonstrating the best multiplicity performance. Figure 7c shows the discharge performance at high and low temperatures, with a discharge rate of 1C and a charging rate of 0.5C. The discharge capacity of each sample is positively correlated with temperature, from −20 to 60 °C. $SiO@C_3H_8@C_2H_2$ consistently exhibits the highest discharge capacity, maintaining 89% of its capacity at −20 °C compared to 25 °C. This

© 2025 Wiley-VCH GmbH

23669608, 2025, 7, Downloaded from https://onlinelibrary.wiley.com/doi/10.1002/smtd.202401829 by Universidade Do Minho, Wiley Online Library on [27/04/2026]. See the Terms and Conditions (https://onlinelibrary.wiley.com/terms-and-conditions) on Wiley Online Library for rules of use; OA articles are governed by the applicable Creative Commons License

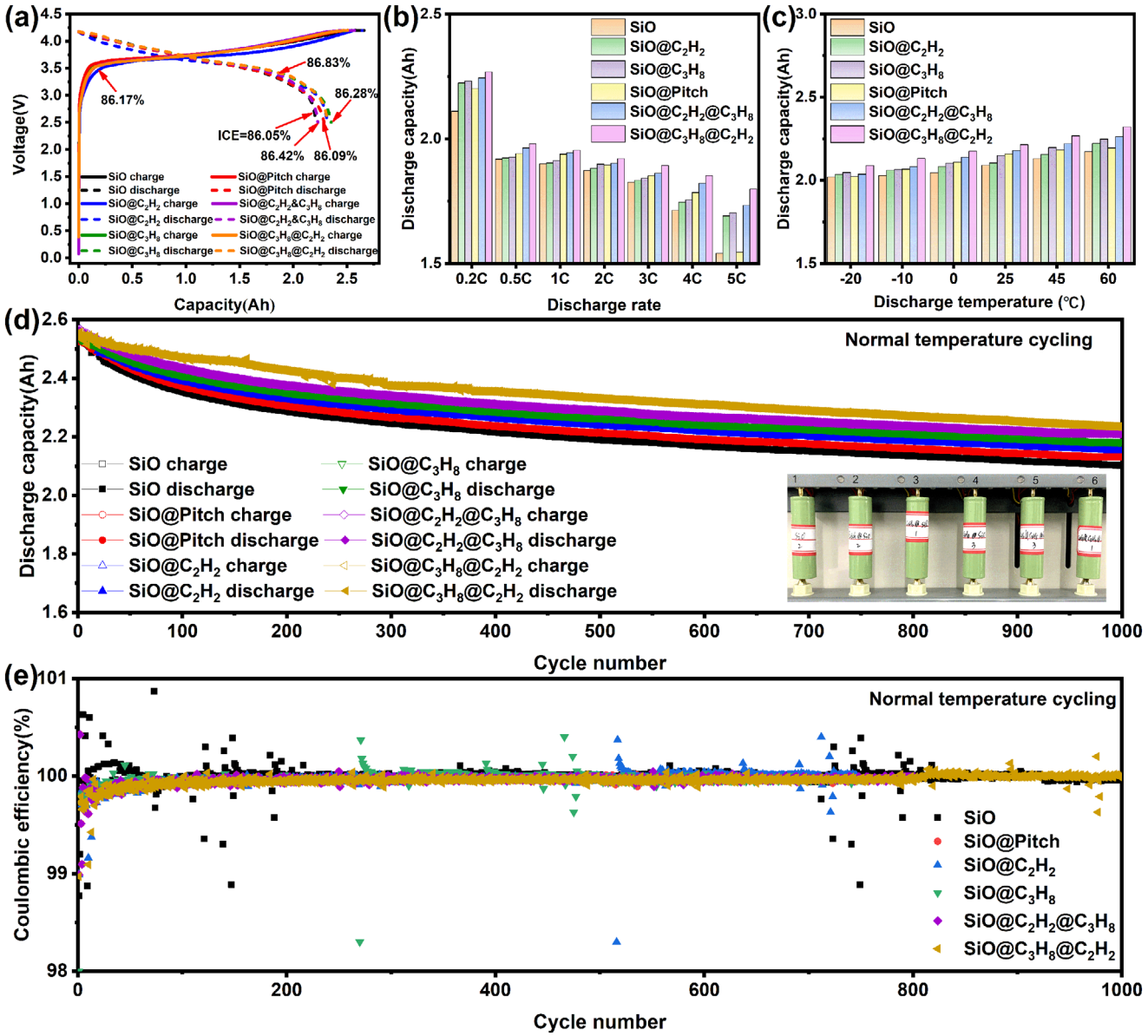


Figure 7. a) First charge and discharge curves, b) Multiplier discharge performance, and c) high and low-temperature discharge performance of all samples. d) Cycling performance and e) Coulomb efficiency of all samples at room temperature (25 °C).

demonstrates the material's robustness suitable for most application scenarios.

Long-cycle tests are crucial for evaluating the cycling stability of the materials. Figure 7d,e shows the discharge capacity and Coulombic efficiency curves of all samples over 1000 cycles at 25 °C, with Figure S6a (Supporting Information) presenting the corresponding capacity retention rates. The charging/discharging current densities are 0.5C. After 1000 cycles, the SiO_X sample shows the lowest discharge capacity (2.1 Ah) and capacity retention (82.8%). Carbon-coated samples demonstrate improved discharge capacity and capacity retention, with $SiO@C_3H_8@C_2H_2$ achieving the best performance (2.2 Ah and 86.6%, respectively). This indicates that the carbon layer significantly enhances cycling performance, with higher-quality carbon layers offering better results. Gas-phase deposited carbon layers are more uniform than solid-phase layers and show superior cycling performance. Successive coating with two gases improves the carbon layer's uniformity, overcoming some limitations of single-gas coatings.

Figure S5a–r (Supporting Information) show the SEM images of the original and after 1000 cycles electrodes of all samples, as well as their cross-sectional topography. From Figure S5g (Supporting Information), it can be obtained that the SEI film on the surface of raw SiOx is not uniform after 1000 cycles, and the local thickest part is ≈83 nm. After carbon encapsulation, the SEI became significantly more homogeneous and the thickness became thinner, where the SEI film thickness of the material encapsulated by a single gaseous carbon source was in the range

© 2025 Wiley-VCH GmbH

23669608, 2025, 7, Downloaded from https://onlinelibrary.wiley.com/doi/10.1002/smtd.202401829 by Universidade Do Minho, Wiley Online Library on [27/04/2026]. See the Terms and Conditions (https://onlinelibrary.wiley.com/terms-and-conditions) on Wiley Online Library for rules of use; OA articles are governed by the applicable Creative Commons License

of 48–50 nm, and that encapsulated by the two gaseous carbon sources successively was in the range of 31–37 nm, which was significantly better than that of 66 nm for the SEI film encapsulated by a solid carbon source. Among them, for the gas-phase methods, it can be concluded that the best quality of the carbon layer on the surface of SiOx, the smaller the SSA, and its SEI film thickness after 1000 cycles is the smallest and also more uniform. This suggests that the uniform carbon layer helps to avoid localized overgrowth of the SEI film, which not only reduces electrolyte consumption but also maintains the basic morphology of the electrode material, thus improving the cycling stability of the cell.

Figure S6b–d (Supporting Information) display the discharge capacity, capacity retention, and Coulombic efficiency over 1000 cycles at 45 °C. The discharge capacity and retention for raw material SiO_X are lowest among all samples at high temperatures, recorded at 2 Ah and 76.6%, respectively). In contrast, $SiO@C_3H_8@C_2H_2$ shows the highest discharge capacity and retention at 2.2 Ah and 83.7%, respectively. Although elevated temperatures enhance the initial discharge capacity, they also accelerate the degradation of active materials and electrode structures, leading to reduced cycling performance compared to room temperature. These results reinforce the notion that a high-quality carbon layer improves cycling performance at elevated temperatures.[49,50]

4. Conclusion

Carbon coating significantly improves the electrochemical properties of SiO_X materials. This study compares the effectiveness of gas-phase and solid-phase carbon coating methods. The solid-phase approach utilizes pitch powder, while gas-phase methods involve C_2H_2 and C_3H_8, both individually and in combination ($C_2H_2@C_3H_8$ and $C_3H_8@C_2H_2$). Key aspects analyzed include the quality of the carbon layers—specifically their surface area, morphology, and internal structure—and how these attributes influence electrochemical performance metrics such as impedance, initial Coulombic efficiency, and cycling stability. The main conclusions are as follows:

1) Carbon coating significantly enhances the electrochemical properties of SiO_X by improving ICE, reducing impedance, and boosting cycling performance. Gas-phase coating methods yield superior results compared to solid-phase methods due to the formation of a homogeneous carbon layer with a smaller SSA and a higher degree of crystallinity.
2) The structure of the deposited carbon layer also affects performance; for instance, carbon from C_2H_2 exhibits a laminar, long-range ordered structure, while that from C_3H_8 is vertically oriented with short-range order. This vertical arrangement facilitates Li-ion migration, making a hybrid coating approach—where vertically oriented grains from C_3H_8 are successively filled by a uniform layer from C_2H_2—particularly effective. The resulting $SiO@C_3H_8@C_2H_2$ sample shows excellent surface quality and electrochemical properties, exhibiting a minimal SSA of 1.14 $m^2\ g^{-1}$, the highest crystallinity, and an impressive ICE of 83.7%. Moreover, it demonstrates an outstanding capacity retention of 86.6% after 1000 cycles at room temperature in a commercial full battery, indicating its significant commercial viability.

In addition to SiO_X anodes, carbon coating is an important technique for enhancing the performance of various other anode materials, including Si-based, Tin-based, and lithium titanate anodes. The low-impedance carbon layer structure presented in this article, along with the characterization and analysis methods, provides valuable guidance for the development of these anodes.

Supporting Information

Supporting Information is available from the Wiley Online Library or from the author.

Acknowledgements

This work was supported by the National Natural Science Foundation of China (No. 51475236 and 51675275). We thank Jiangsu E-ontech company battery company for providing the preparation and testing platform of an 18650-type cylindrical battery. This study forms part of the Advanced Materials program and was supported by MCIN with funding from European Union NextGenerationEU (PRTR-C17.I1) as well as by IKUR Strategy under the collaboration agreement between Ikerbasque Foundation and Fundación BCMaterials on behalf of the Department of Education of the Basque Government. The Fundação para a Ciência e Tecnologia (FCT) is acknowledged for financial support under the framework of Strategic Funding UID/FIS/04650/2020, and under projects 2022.03931.PTDC and c, supported by IAPMEI (Portugal) with funding from the European Union NextGenerationEU (PRR). We also thank the FCT for financial support under contract 2020.04028.CEECIND (DOI 10.54499/2020.04028.CEECIND/CP1600/CT0018) (C.M.C.)

Conflict of Interest

The authors declare no conflict of interest.

Author contributions

X.Z. and M.Z. conceived and designed the experiments, and performed data interpretation. X.Z. and M.Z. carried out the main experiments and data analysis; J.Z. assisted with the preparation and test of half cells. X.Z. supported the preparation and test of full cells. X.Z., M.Z., CM.C, F.S., SL.M., W.W., and Q.Z. co-wrote the paper.

Data Availability Statement

The data that support the findings of this study are available in the supplementary material of this article.

Keywords

CVD method, impedance, layered carbon structure, SiO_X, vertical carbon structure

Received: October 29, 2024
Revised: December 28, 2024
Published online: January 16, 2025

© 2025 Wiley-VCH GmbH

23669608, 2025, 7, Downloaded from https://onlinelibrary.wiley.com/doi/10.1002/smtd.202401829 by Universidade Do Minho, Wiley Online Library on [27/04/2026]. See the Terms and Conditions (https://onlinelibrary.wiley.com/terms-and-conditions) on Wiley Online Library for rules of use; OA articles are governed by the applicable Creative Commons License

[1] Y. Cui, *Nature Energy*. **2021**, *6*, 995.
[2] Y. Liang, C.-Z.i Zhao, H. Yuan, Y. Chen, W. Zhang, J.-Q. Huang, D. Yu, Y. Liu, M.-M. Titirici, Y.-L. Chueh, H. Yu, Q. Zhang, *InfoMat* **2019**, *1*, 6.
[3] G. Crabtree, *Science* **2019**, *366*, 422.
[4] C. C. Li, Y. W. Wang, *J. Power Sources* **2013**, *227*, 204.
[5] H. Wang, M. Yoshio, T. Abe, Z. Ogumi, *J. Electrochem. Soc.* **2002**, *149*, A499.
[6] M. Zhao, J. Zhang, X. Zhang, K. Duan, H. Dong, S. Lanceros-Méndez, W. Wang, Q. Zhang, *Energy Storage Mater.* **2023**, *61*, 102857.
[7] H. Chen, G. Xu, C. Jin, J. Wu, L. Xiong, X. Li, F. Sun, L. Zhou, Z. Yue, *Mater. Lett.* **2023**, *341*, 134192.
[8] J. Xiong, G. Xiang, Z. Lei, V. Florian, X. Yuzheng, L. Mingzhu, X. Caihong, Z. Zongbo, *J. Mater. Sci.* **2023**, *58*, 1656.
[9] Y. Yixue, H. Qiang, Z. Guimin, X. Xun, L. Yuxin, Z. Liming, W. Kejing, L. Houfang, L. Bin, *Energy Fuels* **2023**, *37*, 7973.
[10] W. J. Zhang, *J. Power Sources* **2011**, *196*, 13.
[11] W. He, Y. Liang, H. Tian, S. Zhang, Z. Meng, W.-Q. Han, *Energy Storage Mater.* **2017**, *8*, 119.
[12] Z. Cao, P. Xu, H. Zhai, S. Du, J. Mandal, M. Dontigny, K. Zaghib, Y. Yang, *Nano Lett.* **2016**, *16*, 7235.
[13] H. Li, Z. Wang, L. Chen, X. Huang, *Adv. Mater.* **2009**, *21*, 4593.
[14] H. Yamamura, K. Nobuhara, S. Nakanishi, H. Iba, S. Okada, *J. Ceramic Soc. Japan* **2011**, *119*, 855.
[15] S. Yoon, H. S. Kim, S. G. Pyo, *2019 IEEE Asia-Pacific Conf. on Computer Science and Data Engineering (CSDE)*, Melbourne, VIC, Australia, December, **2019**.
[16] X. Zhang, M. Zhao, J. Zhang, J. Lei, W. Wang, Q. Zhang, *J. Energy Storage* **2024**, *83*, 110659.
[17] D. Sui, M. Yao, L. Si, K. Yan, J. Shi, J. Wang, C. C. Xu, Y. Zhang, *Carbon* **2023**, *205*, 510.
[18] H. Lee, D. J. Lee, M. Kim, H. Kim, Y. S. Cho, H. J. Kwon, H. C. Lee, C. R. Park, D. Im, *ACS Appl. Mater. Interfaces* **2020**, *12*, 17385.
[19] B. Chan, A. Karton, *Phys. Chem. Chem. Phys.* **2021**, *23*, 17713.
[20] E. López-Honorato, P. J. Meadows, P. Xiao, *Carbon* **2009**, *47*, 396.
[21] K. Norinaga, O. Deutschmann, K. J. Hüttinger, *Carbon* **2006**, *44*, 1790.
[22] M. DB, R. W. Carroll, J. E. Klonowski, *Carbon* **1997**, *35*, 1819.
[23] S. J. C. Cassady, R. Boddapati, N. H. D. VivekPinkowski, D. F. Hanson, K. Ronald, *Int. J. Chem. Kinet.* **2020**, *52*, 725.
[24] M. Yuan, C. Meng, A. Li, B. Cao, Y. Dong, D. Wang, X. Liu, X. Chen, H. Song, *Small* **2022**, *18*, 2105738.
[25] J. Li, S. Yang, X. Zhang, C. Zhang, *Comput. Theor. Chem.* **2022**, *1217*, 113937.
[26] X. Shi, Y. Zhang, G. Xu, S. Guo, S. Liang, *Sci. Bull.* **2020**, *65*, 2014.
[27] H. Wang, P. Wu, H. Shi, W. Tang, Y. Tang, Y. Zhou, P. She, T. Lu, *J. Power Sources* **2015**, *274*, 951.
[28] Z. Yuan, N. Zhao, C. Shi, E. Liu, C. He, F. He, *Chem. Phys. Lett.* **2016**, *651*, 19.
[29] C. Qi, S. Li, Z. Yang, Z. Xiao, L.u Zhao, F. Yang, G. Ning, X. Ma, C. Wang, J. Xu, J. Gao, *Carbon* **2022**, *186*, 530.
[30] J. Zhao, B. Rui, W. Wei, P. Nie, L. Chang, X. Xue, L. Wang, J. Jiang, *J. Colloid Interface Sci.* **2021**, *11*, 1850067.
[31] G. Hou, B. Cheng, Y. Yang, Y. Du, F. Yuan, *ACS Nano* **2019**, *13*, 10179.
[32] M. Tello, A. R. Garce, *Appl. Phys. Lett.* **2003**, *83*, 2339.
[33] N. Y. Kim, P. E. Laibinis, *J. Am. Chem. Soc.* **1997**, *119*, 2297.
[34] W. Wu, Y. Liang, H. Ma, Y. Peng, H. Yang, *Electrochim. Acta* **2016**, *187*, 473.
[35] Y. Yu, J. Zhang, L. Xue, H. Tao, A. Yu, *J. Power Sources* **2011**, *196*, 10240.
[36] S. S. Zhang, K. Xu, T. R. Jow, *Electrochim. Acta* **2006**, *51*, 1636.
[37] B. Zhang, L. Wang, Y. Zhang, X. Wang, Y. Qiao, S. G. Sun, *J. Chem. Phys.* **2023**, *158*, 054202.
[38] J. Guo, A. Sun, X. Chen, C. Wang, A. Manivannan, *Electrochim. Acta* **2011**, *56*, 3981.
[39] L.i Mingqi, Y. Zuolong, H. Xiaoying, *Electrochim. Acta* **2010**, *55*, 2217.
[40] M. Xia, Y. Li, Z. Zhou, Y. Wu, N. Zhou, H. Zhang, X. Xiong, *Ceram. Int.* **2019**, *45*, 1950.
[41] Q. Sun, J. Li, M. Yang, S. Wang, G. Zeng, H. Liu, J. Cheng, D. Li, Y. Wei, P. Si, Y. Tian, L. Ci, *Small* **2023**, *19*, 1.
[42] Y. S. Meng, A. D. Dompablo, *Energy Environ. Sci.* **2009**, *2*, 589.
[43] V. L. Chevrier, J. W. Zwanziger, J. R. Dahn, *Can. J. Phys.* **2009**, *87*, 625.
[44] M. S. Park, Y. M. Kang, G. X. Wang, S. X. Dou, H. K. Liu, *Adv. Funct. Mater.* **2008**, *18*, 455.
[45] D. Wang, C. Zhou, B. Cao, Y. Xu, H. Song, *Energy Storage Mater.* **2019**, *24*, 312.
[46] G. Chuanhai, Z. Chengkun, W. Weidong, L. Yingkuan, C. Juan, X. Qingshui, L. Xuetao, *ACS Appl. Mater. Interfaces* **2019**, *11*, 35809.
[47] J. Chang, X. Huang, G. Zhou, S. Cui, P. B. Hallac, J. Jiang, P. T. Hurley, J. Chen, *Adv. Mater.* **2014**, *26*, 758.
[48] B. D. Polat, O. Keles, *J. Power Sources* **2014**, *266*, 353.
[49] G. Zhu, Y. Wang, S. Yang, Q. Qu, H. Zheng, *J. Materiomics* **2019**, *5*, 164.
[50] R. Malik, D. Burch, M. Bazant, G. Ceder, *Nano Letters.* **2010**, *10*, 4123.

© 2025 Wiley-VCH GmbH

23669608, 2025, 7, Downloaded from https://onlinelibrary.wiley.com/doi/10.1002/smtd.202401829 by Universidade Do Minho, Wiley Online Library on [27/04/2026]. See the Terms and Conditions (https://onlinelibrary.wiley.com/terms-and-conditions) on Wiley Online Library for rules of use; OA articles are governed by the applicable Creative Commons License